Sustainable Energy & Fuels

ROYAL SOCIETY OF CHEMISTRY

PAPER

View Article Online
View Journal | View Issue

Cite this: *Sustainable Energy Fuels*, 2026, **10**, 2245

Ionic liquid-engineered core–shell polymer nanospheres for photocatalytic nitrogen reduction

Ning Zhang,[a] Dorian Priano,[a] Catherine Santini,[a] Jinlong Zhang[b] and Stephane Daniele*[a]

Resorcinol–formaldehyde resin (RF), a novel organic photocatalytic material, has seen extensive application in the photocatalytic generation of hydrogen peroxide in recent years, owing to its broad band gap structure and robust visible light absorption capabilities. The favorable positions of the conduction and valence bands of RF theoretically enable RF application in photocatalytic nitrogen fixation. Nevertheless, the limited solubility of nitrogen in water results in diminishing the effectiveness of photocatalytic nitrogen fixation. Herein, we present a method to coat RF nanospheres with an ionic liquid (RF@IL) exhibiting significant nitrogen enrichment capacity to develop a novel organic semiconductor material featuring a core–shell configuration. The abundant hydroxyl functional groups on the surface of RF nanospheres facilitate the coating of imidazolium ionic liquids, affording a nitrogen-rich thin film for the RF nanospheres and segregate the sites of nitrogen reduction and water oxidation, minimizing the recombination of photogenerated carriers and thereby enhancing the efficacy of the photocatalytic nitrogen fixation reaction. RF@IL facilitated photocatalytic nitrogen fixation, yielding 58.7 μmol g^{-1} of ammonia in 2 hours, which is 1.80 times greater than the blank RF output of 32.6 μmol g^{-1}. Remarkably, after five testing cycles, RF@IL retains substantial photocatalytic ammonia synthesis activity, underscoring the considerable influence of ionic liquids on photocatalytic processes. This study offers a viable solution to the issue of low nitrogen solubility impacting reaction performance in photocatalytic nitrogen fixation experiments.

Received 22nd December 2025
Accepted 18th March 2026

DOI: 10.1039/d5se01680k

rsc.li/sustainable-energy

1 Introduction

Ammonia (NH_3) is an essential component in the production of agricultural fertilizers and synthetic fabrics.[1] The conversion of N_2 to NH_3 ($2N_2 + 6H_2O \rightarrow 4NH_3 + 3O_2$) is extremely challenging due to the high N≡N bond energy (945 kJ mol^{-1}) and needing the transfer of many electrons and protons.[2,3] Recent years have witnessed a surge in studies on photocatalytic and photoelectrocatalytic reactions harnessing solar energy, including the catalytic decomposition of water to generate hydrogen and oxygen,[4] and the reduction of CO_2 to produce fuel.[5] Consequently, an increasing number of scientists have started to focus on the domain of the photocatalytic nitrogen reduction reaction (PCNRR).[6] Recent successful PCNRR conducted under mild environmental circumstances, leading to a substantial decrease in carbon dioxide emissions, presents an attractive alternative to the Haber–Bosch method for ammonia production.[7–11]

However, the use of inexpensive, highly active, and easy to produce materials is critical for the development of any photocatalytic process. Organic photocatalytic compounds are less expensive, such as C_3N_4[12,13] and MOF,[14,15] have a simpler preparation procedure, and are often more stable than standard metal photocatalytic materials. Furthermore, the surface chemical characteristics of organic photocatalytic materials can be adjusted at the molecular level by altering the precursors, resulting in improved photocatalytic performance.

Nevertheless, all nitrogen-based photocatalysts can yield false positive results in photocatalytic investigations due to various critical aspects associated with their chemical composition, electrical characteristics, and interactions with the reaction environment. So, the 1,3-benzenediol (resorcinol)–formaldehyde resin (RF) developed by Professor Pekala in 1989 is an inexpensive molecular cross-linked polymer produced by using a low-temperature hydrothermal process (298–373 K).[16] As an advanced organic semiconductor, RF has garnered widespread attention in photo-degradation[17] and photocatalytic hydrogen production.[18] Especially, Professor Shiraishi *et al.* employed RF as an effective organic photocatalytic material to generate H_2O_2,[19] further enabling the wider application of non-metallic, simple-to-synthesize, and stable RF in the field of photocatalysis.

[a]*Universite Lyon 1, CP2M-ESCPE Lyon, CNRS-UMR 5128, 69616 Villeurbanne Cedex, France. E-mail: stephane.daniele@univ-lyon1.fr*

[b]*Key Laboratory for Advanced Materials, Institute of Fine Chemicals, East China University of Science and Technology, 130 Meilong Road, Shanghai 200237, P. R. China. E-mail: jlzhang@ecust.edu.cn*

Moreover, significant cost reductions could be achieved by performing the PCNRR in water, which serves as the proton source to reduce activated nitrogen and generate NH_3. Despite this promise, aqueous PCNRR faces significant challenges that drastically lower NH_3 yields, one of which is the low N_2 solubility in water (~0.5 mmol L^{-1} at 25 °C, 1 bar).[20] Enhancing nitrogen solubility in the process can substantially impact the efficacy of the PCNRR. Over the past decade, ionic liquids (ILs) have shown promising advantages as alternatives to water (including excellent gas absorption capabilities, negligible vapor pressure, and chemical and thermal stability).[21] Research towards the vision of green ammonia has intensified, with ILs not only serving as electrolytes with a higher nitrogen solubility,[22,23] but also playing a crucial role as proton carriers.[24,25]

Moreover, ILs have demonstrated significant potential in the field of photocatalysis. The functional groups of ionic liquids, including the imidazolium ring, amino group, and sulfur group, establish charge transfer complexes with the semiconductor surface, thereby introducing intermediate energy levels and reducing the effective band gap.[26] Heteroatoms (N, S, F, *etc.*) in ionic liquids infiltrate the semiconductor lattice, establishing doping energy levels and altering the electrical structure.[27] Because of their stable qualities and ease of availability, the use of imidazolium ionic liquids has become a popular research topic in the photocatalytic reduction reaction: (i) as solvent[20,28,29] and (ii) as a photocatalyst modifier, Chen *et al.* developed visible light sensitive S^{6+} doped TiO_2 nanocatalysts (S–TiO_2) using water or a ionic liquid $[C_1C_4im]PF_6$ as reaction media. The results demonstrated that the $[C_1C_4im]PF_6$ ionic liquid used as an auxiliary solvent did not easily volatilize during the procedure. The S–TiO_2 sample had a larger specific surface area and higher photocatalytic activity than the water-prepared sample.[30] Golabiewska *et al.* discovered that 1,2-dimethyl-3-octadecyl imidazolium chloride ($[C_1C_1C_8im]Cl$) promoted the solvothermal production of TiO_2 microspheres. The results revealed that the interaction of the ions in the ionic liquid with the surface of the developing titanium dioxide spheres caused the absorption edge of IL-TiO_2 to red shift. Compared to blank TiO_2, IL-TiO_2 significantly increased the degrading impact of the phenol solution.[31] Finally, an imidazolium-based ionic liquid was used as a homogeneous catalyst for the photocatalytic reduction of CO_2 to CO in both iPrOH and H_2O media.[32]

In this work, we successfully grafted an ionic liquid [1-(3-bromopropyl)-3-methyl-1*H*-imidazol-3-ium bromide] onto the surface of blank RF under solvothermal conditions at 120 °C for 3 days, resulting in the formation of core–shell systems RF@IL. The structure of RF@IL was confirmed by several spectroscopic analyses (FT-IR, TEM, and FESEM mapping); then RF@IL was tested in photocatalytic nitrogen fixation.

2 Experimental

2.1 Materials

Resorcinol (C_6H_4-1,3-$(OH)_2$, 99%), formaldehyde (HCHO, 37%), potassium sodium tartrate $KOCOCH(OH)CH(OH)COONa\cdot 4H_2O$, 99%), salicylic acid (2-$(HO)C_6H_4CO_2H$, 99%), sodium citrate ($HOC(COONa)(CH_2COONa)_2\cdot 2H_2O$, 99%), sodium nitroprusside ($Na_2[Fe(CN)_5NO]\cdot 2H_2O$, 99%), sodium hypochlorite solution (NaClO, 10%), maleic acid ($HO_2CCH{=}CHCO_2H$, 99%), dimethyl sulfoxide-d_6($(CD_3)_2SO$, 99.9%), hydrazine monohydrochloride (NH_2NH_2 2HCl, 98%), 4-dimethylaminobenzaldehyde ($C_9H_{11}NO$, 98%), hydrochloric acid (HCl, 37%), and methanol (CH_3OH, 99.9%) were purchased from Sigma-Aldrich. All reagents were of analytical grade and used without further purification.

2.2 Preparation of [1-(3-bromopropyl)-3-methyl-1*H*-imidazol-3-ium bromide]

As described in the literature,[33] 10.357 mL of 1,3-dibromopropane (0.102 mol) were mixed with 30 mL of acetone until it completely dissolves. An acetone solution (10 mL) containing 0.829 mL of 1-methylimidazole (0.01 mol) was added to the media. The mixture was then stirred at a temperature of 50 °C for 24 hours under argon.

Then, the solvent was evaporated, and the crude product was purified by washing with diethyl ether (30 mL). The product (mixture of monomer and dimer) was obtained as a white solid. The crude product was dissolved in 40 mL of dichloromethane and stirred for 24 h, allowing the separation of the monomer (experimental weight = 0.728 g; yield: 25.6%).

^{1}H-NMR (300 MHz, CD_2Cl_2) δ (ppm): 10.43 (1H, s, N–CH–N),7.43 (1H, s, N^+-CH-CH), 7.32 (1H, s, N–CH–CH), 4.49 (2H, t, N–CH_2–CH_2), 3.99 (3H, s, N^+-CH_3), 3.44 (2H, t, CH_2–CH_2–Br), 2.48 (2H, q, CH_2–CH_2–CH_2).

^{13}C NMR (300 MHz, CD_2Cl_2) δ (ppm): 137.95 (s, N–CH–N^+), 124.01 (s, CH–CH–N^+), 123.02 (s, CH–CH–N), 48.60 (s, N–CH_2–CH_2), 37.14 (s, $^+$N–CH_3), 33.22 (s, CH_2–CH_2–CH_2), 30.04 (s, CH_2–CH_2–Br).

IR: 3065 cm^{-1} imidazole ring (νC–H), 1562 cm^{-1} imidazole ring stretching, 1162 cm^{-1} HC–C and HC–N bending, 840 cm^{-1} in-plane bending stretching of the imidazole ring, 763 cm^{-1} out-of-plane C–H bending of the imidazole ring, and 620 cm^{-1} imidazole C2–N1–C5 bending.

ESI$^+$ m/z (M^+): doublet same intensity 203 & 205 [^{79}Br$(CH_2)_3$-ImCH_3]$^+$ & [^{81}Br$(CH_2)_3$ImCH_3]; ESI$^-$ m/z (A^-): doublet same intensity 78.9 (^{79}Br) & 80.9 (^{81}Br)

2.3 Preparation of resorcinol–formaldehyde resin RF-110

RF was prepared by the conventional Stöber method.[34]

At room temperature, a solution of 8 mL of anhydrous ethanol and 20 mL of deionized water was stirred for 10 min. To this was added 1.20 g of resorcinol and the mixture was stirred continuously for 30 min. Then, 1.68 mL of formaldehyde solution was added and kept under stirring at 110 °C for 72 h. A solid product was formed and collected by centrifugation (10 000 rpm). After three washings with deionized water and ethanol (20 mL and 20 mL, respectively), it was dried in an oven at 70 °C for 12 h affording a light red solid product (experimental weight: 0.8596 g, yield: 54.4%) referred to as RF-110.

2.4 Preparation of RF-110@IL

K_2CO_3 (333.8 mg, 2.4 mmol) and 1-(3-bromopropyl)-3-methyl-1*H*-imidazol-3-ium bromide (681.6 mg, 2.75 mmol) were

dissolved in dry DMF (30 mL) under an argon atmosphere, and then RF-110 (100 mg) was added. The mixture was heated at 120 °C and stirred for 36 h. The product was isolated and washed with methanol and then dried under vacuum (10^{-3} mmHg), affording a dark-brown solid (experimental weight = 0.276 g; yield: 35.3%) in the glove box. The structure of RF@IL was confirmed by several spectroscopic analyses (FT IR, TEM, and FESEM mapping)

2.5 Ammonia detection methods

As shown in SI Fig. S12–S15 analysis, two separate ammonia detection methods, the Nessler reagent method and the indophenol blue method, were utilized to detect the ammonia produced by the photocatalytic reaction, giving the experimental results greater credibility.

2.6 Photocatalytic nitrogen fixation test

In the experimental apparatus shown in SI Fig. S1, 50 mg of catalyst is weighed and ultrasonically dispersed in 100 mL of deionized water. The reaction solution is then transferred to a 150 mL photocatalytic reactor and stirred continuously to ensure uniform mixing. To eliminate dissolved oxygen from the solution, high-purity nitrogen (99.99%) is bubbled through it for 30 minutes at a controlled flow rate of 20 mL per minute. Once the degassing process is complete, the xenon lamp is switched on to irradiate the reaction mixture. If necessary, an appropriate filter can be applied to the lamp head to eliminate unwanted light in specific wavelength bands (only visible light 305–780 nm was used in this reaction).

Every 10 min (after 1 hour, every 30 min), an aliquot of 6 mL of liquid was removed and centrifuged at 11 000 rpm to separate solid residues, and then the supernatant was filtered using a syringe equipped with a 0.22 μm microporous filter membrane. From the filtered solution, 5 mL was analysed, and after that a specific detection reagent was added. The absorbance of the final solution was then measured at a fixed wavelength using a UV spectrophotometer to determine the reaction's progress. The total reaction time for the experiment was set to 2 hours.

2.7 Ammonia detection procedures

The identification of synthesized ammonia in the photocatalytic nitrogen fixation process utilizes UV spectrophotometry. The Nessler reagent method utilizes ammonia nitrogen as free ammonia or ammonium ions, which react with Nessler's reagent to form a light reddish-brown complex. The absorbance of the complex correlates with its ammonia nitrogen content and is quantified at 420 nm. The standard curve is constructed using ammonium chloride [see SI Fig. S12–S15].

3 Results and discussion

The resorcinol–formaldehyde resin (RF-110) was synthesized following the conventional Stöber method at 110 °C. The microstructure, chemical structure, and electrochemical characteristics of the catalyst were investigated.

To increase the nitrogen adsorption, RF-100 was modified with an ionic liquid 1-(3-bromopropyl)-3-methyl-1*H*-imidazol-3-ium bromide (681.6 mg, 2.75 mmol) to afford a product referred to as RF-110@IL. The structures of both materials were analyzed by XPS, FESEM mapping, EDX, and FT-IR. Fig. 1A and B depict SEM and TEM images of the RF-100 nanospheres, whereas Fig. 1H and I display those of RF-110@IL, both exhibiting a smooth surface and a uniform size around 500 nm. Consequently, the IL grafting did not impact the morphology and architecture of RF-110 nanospheres.

The EDS spectrum of RF-110 (Fig. 1C) indicated that two elements, C and O, are in atomic ratios of 88.90 : 11.10, respectively and that no nitrogen atom is present. In contrast, the EDS spectrum of RF-110@IL (Fig. 1J) showed the presence of three elements: carbon, nitrogen, and oxygen in atomic ratios of 95.93 : 0.01 : 4.46, respectively. Compared to RF-110, the atomic fraction of the carbon element increases while that of the oxygen element drops. This could be attributed to the grafting of ionic liquids, which introduces a significant number of carbons. At the same time, nitrogen with an atomic content of 0.01 was detected in RF-110@IL. According to the analysis of different chemicals added during the experiment, the only source of nitrogen was the ionic liquid (1-(3-bromopropyl)-3-methyl-1*H*-imidazol-3-iumbromide), demonstrating its presence on the surface of RF-110.

Fig. 1K–O depicts the element distribution of the final RF-110@IL. We employed a high-precision HAADF electron microscope to discover that, at a scale of 50 nm, when the ionic liquid was grafted with RF-110, a thin layer of other substances appeared on the surface of the nanospheres, which should be the ionic liquid. At the same time, due to the ionic liquid's adhesive capabilities, nanospheres gathered in vast quantities beneath the microstructure, making it difficult to locate a thin layer of ionic liquid on the surface. The figures show that carbon, oxygen, and nitrogen are uniformly spread in the nanostructure of RF@IL, whereas pure RF does not include nitrogen (as shown in Fig. 1D–G). The element types are compatible with the EDS spectrum results, demonstrating that in the produced nanomaterials, IL was successfully grafted onto the surface of RF. Following IL grafting, nitrogen components found solely in IL were identified in the nanostructure of RF-110@IL.

Photocatalysts have a large BET surface area, and a mesoporous structure can facilitate N_2 adsorption and activation reactions on their surface. As a result, the BET surface area and porosity of the produced photocatalyst were evaluated by measuring the N_2 adsorption–desorption isotherm. Fig. 2A and C show that both RF-110 and RF-110@IL exhibit type IV isotherms, indicating that they have mesoporous architectures. RF-110@IL possesses an H3-type hysteresis loop, indicating the presence of slit-like pores in the material, possibly induced by nanosphere buildup. As shown in Fig. 2, the BET surface area of RF-110 is 10.58 $m^2\ g^{-1}$, while that of RF-110@IL is reduced to 5.21 $m^2\ g^{-1}$. Similarly, the pore volume significantly decreases from 0.0278 $cm^3\ g^{-1}$ for RF-110 to 0.0072 $cm^3\ g^{-1}$ for RF-110@IL, representing a 3.8-fold reduction. To further clarify the origin of this reduction, an 'apparent' BET value ($S_{apparent}$)

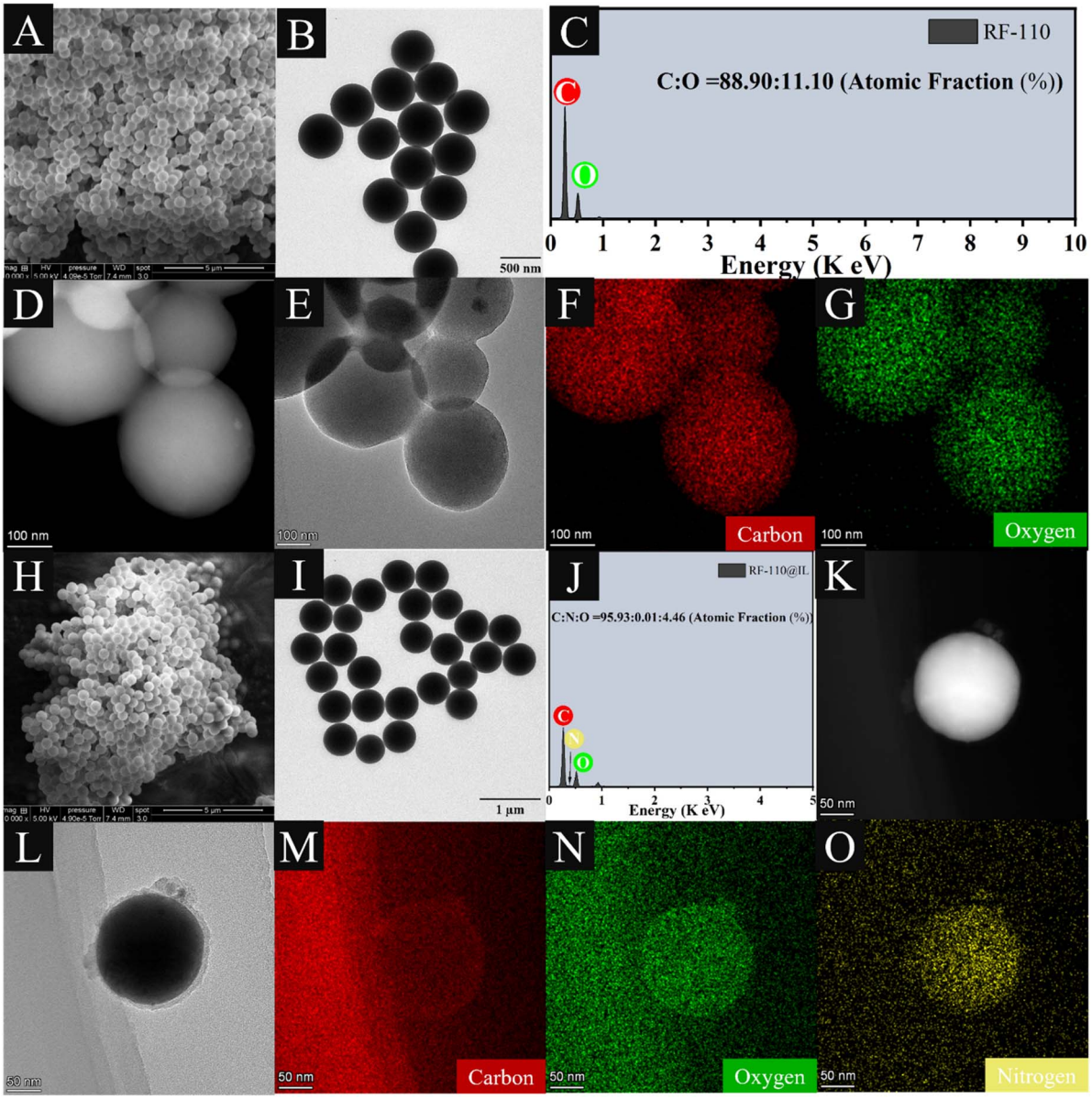

Fig. 1 (A) SEM image for RF-110; (B) TEM image for RF-110; (C) EDS spectra of RF-110; (D) HAAD-STEM image for RF-110; (E–G) STEM element mapping images for RF-110; (H) SEM image of RF-110@IL; (I) TEM image of RF-110@IL; (J) elemental analysis image of RF-110@IL; (K) HAADF image of RF-110@IL; (L–O) element distribution image of RF-110@IL.

was calculated based solely on the mass of the RF-110 core, thereby excluding the weight contribution of the IL shell. As shown in Table S4, given the IL weight fraction ($Z = 18.5\%$) derived from the molecular structure of the IL and the re-analyzed EDX data, the $S_{apparent}$ was determined to be 6.39 m^2 g^{-1}. Since this recalculated value remains significantly lower than the original surface area of bare RF-110 (10.58 m^2 g^{-1}), it is concluded that the loss in surface area and pore volume is primarily driven by the physical pore-filling and blocking effect of the liquid-like IL shell rather than a mere weight-dilution effect. The high viscosity of the ionic liquid causes the nanospheres to stack and its molecules to occupy the microporous channels of the RF core, effectively reducing the accessible area for N_2 molecules during measurements.

FT-IR spectroscopy was used to analyse the functional groups of the synthesized ionic liquid (SI Fig. S2–S9) to confirm the above experimental data. We successfully synthesized the monomer. Fig. 3A and S10 show the infrared spectra of RF-110. The band at 3300 cm^{-1} corresponds to the O–H functional group in resorcinol or methylol; the one at 2925 cm^{-1} is attributed to the C–H bond in the methylene linker; the band at 1700 cm^{-1} corresponds to the C=O bond in the –CHO residue; the band at 1620 cm^{-1} corresponds to the C=C bond in the aromatic ring; the bands at 1490 cm^{-1} and 1450 cm^{-1} are due to the C–H bond in the methylene linker; the bands at 1370 cm^{-1} and 1300 cm^{-1} are attributed to the C–H bond in the aromatic ring; and finally the bands at 1240 cm^{-1} and 1100 cm^{-1} correspond to the C–O bond in resorcinol and methylol,

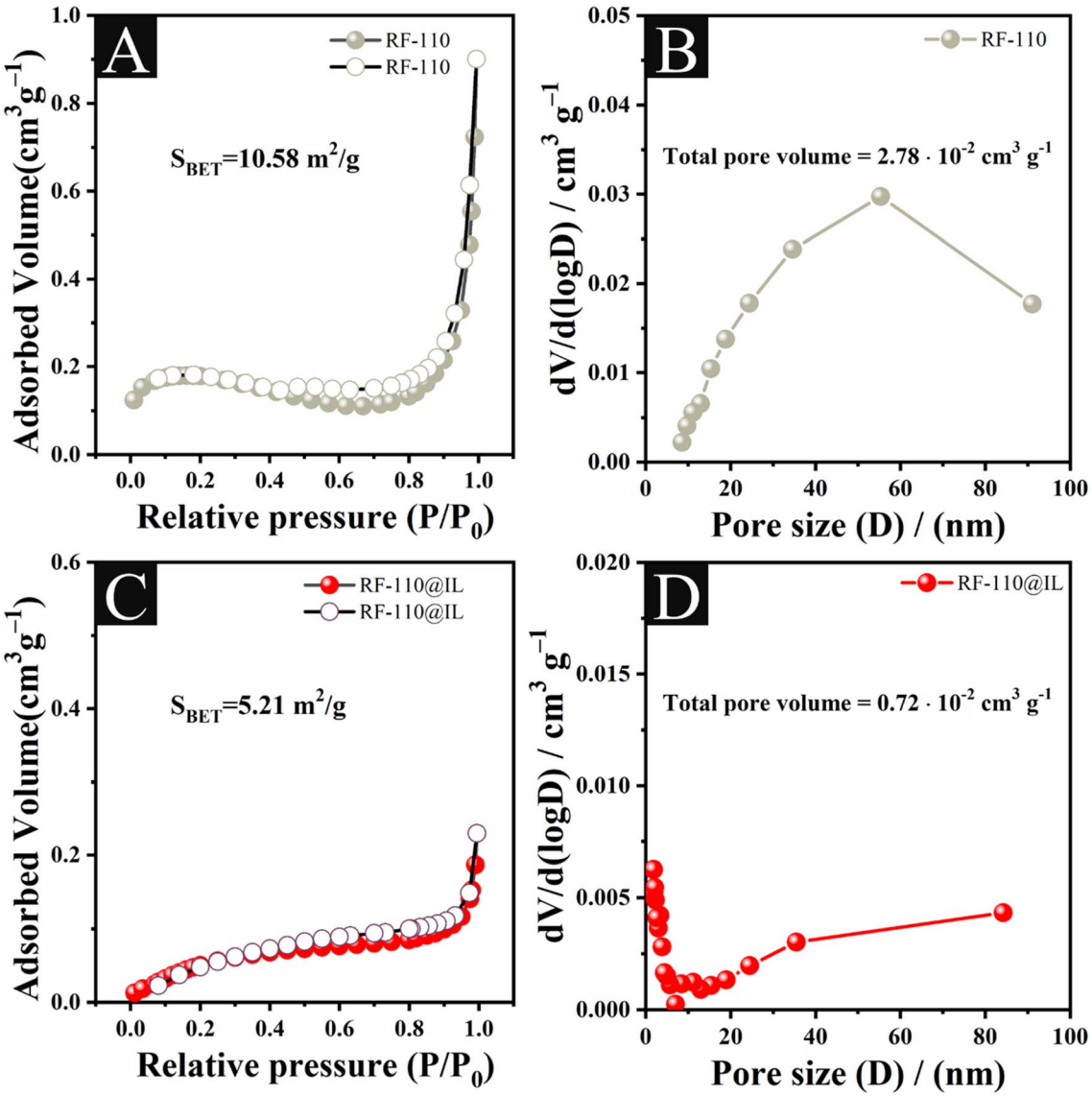

Fig. 2 (A) N_2 adsorption/desorption isotherms of RF-110. (B) Pore size distribution curves of RF-110. (C) N_2 adsorption/desorption isotherms of RF-110@IL. (D) Pore size distribution curves of RF-110@IL.

respectively.[35] Fig. 3B and S11 show the infrared spectra of RF-110@IL. A new band appeared at 1050 cm^{-1}, likely due to the aromatic–oxygen (R–O) bond on the benzene ring formed by the substitution process of bromine atoms and hydroxyl groups, as shown in Fig. 3C and D.

Simultaneously, by comparing with the infrared spectrum of IL, the band at 3065 cm^{-1} is due to the imidazole ring (νC–H); the one at 1562 cm^{-1} is attributed to imidazole ring stretching, and that at 1162 cm^{-1} for HC–C and HC–N bending. The band at 840 cm^{-1} corresponds to the in-plane bending stretching of the imidazole ring, and that at 763 cm^{-1} corresponds to the out-of-plane C–H bending of the imidazole ring. The absorption at 620 cm^{-1} is related to the imidazole C2–N1–C5 bending.

As a result of the infrared analysis of RF-110@IL and comparison with RF-110 and ionic liquids, we can conclude that the ionic liquid was successfully grafted onto the surface of RF-110 using our experimental approach, which is compatible with the FESEM mapping results.

The full XPS spectra of RF-110 and RF-110@IL (Fig. 4A) show that the RF-110 nanomaterial contains only carbon and oxygen while RF-110@IL has three elements: carbon, oxygen, and nitrogen.

Fig. 4B–E depicts the high-resolution XPS spectra for the elements C and O in RF-110 and RF-110@IL, respectively. The peaks of the C 1s orbital are made up of two components: C=O and C–O. Among them, the peak at 284.6 eV belongs to the carbon-oxygen double bond, whereas the peak at 286.2 eV corresponds to the single bond. The peak at 288.3 eV corresponds to the sp^2-bonded carbon (N–C–N).[36] The peaks of the O 1s orbital can be attributed to two components: C=O and C–O. Among these, the peak at 531.4 eV represents the carbon-oxygen double bond, whereas the peak at 533.0 eV represents the

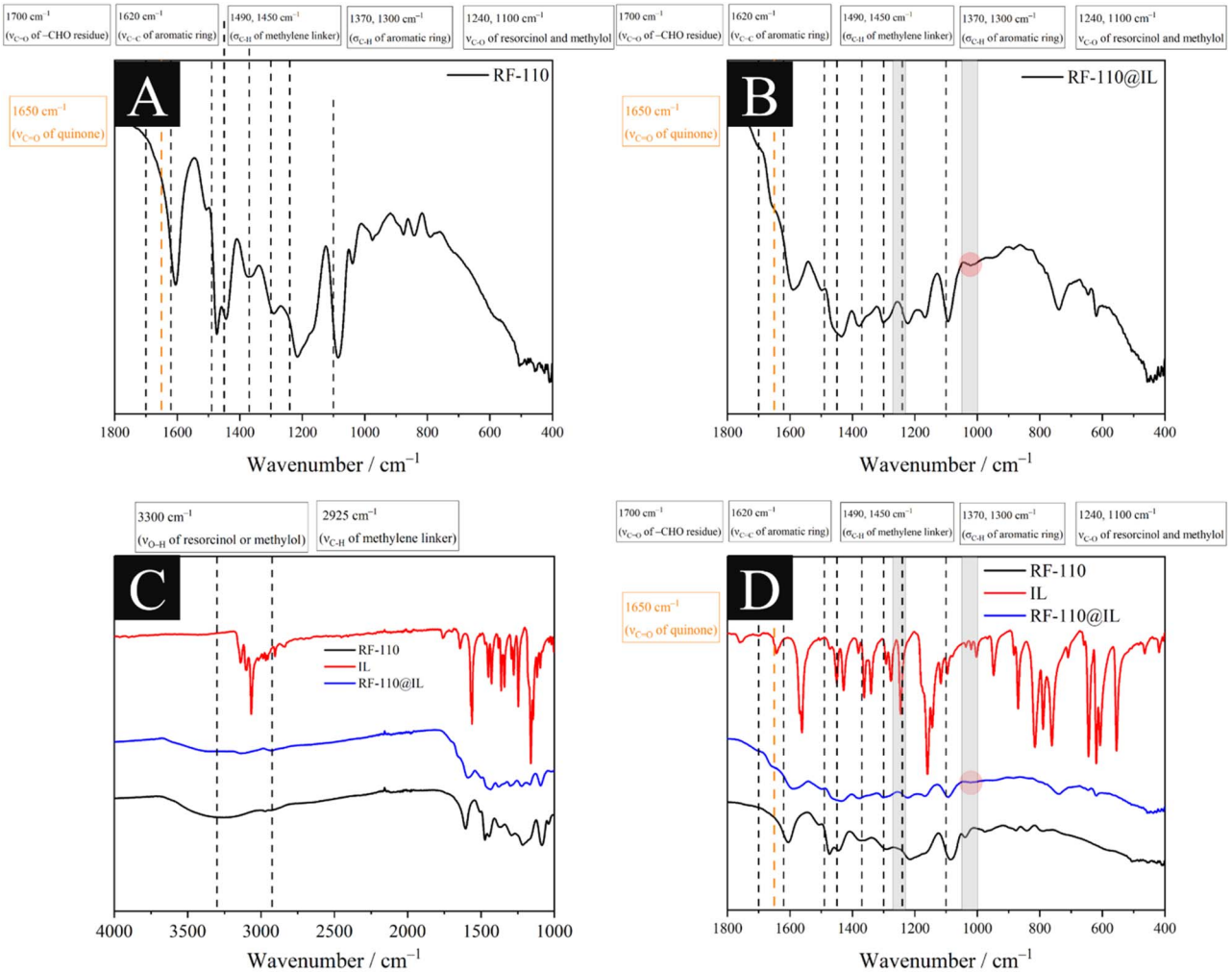

Fig. 3 (A) FT-IR spectrum of RF-110; (B) FT-IR spectrum of RF-110@IL (monomer); (C and D) FT-IR spectra of IL, RF-110 and RF-110@IL.

carbon-oxygen single bond.[18] Fig. 4F shows the high-resolution XPS spectra for the N 1s orbital in RF-110@IL. The peak at 401 eV belongs to the N of the imidazolium cation[37] confirming the presence of ILin RF-110@IL. The experimental results are consistent with those of FESEM mapping and EDS.

As shown in Fig. S16, ammonia synthesis occurs only in the presence of catalysts, high-purity nitrogen, water, and light, proving that RF-110 can be used for photocatalytic ammonia synthesis. A small amount of ammonia also occurs when ambient air is bubbled, as air contains 78% nitrogen. Notably, no ammonia was detected in control experiments conducted under an Ar atmosphere (Fig. S17), proving that neither the IL nor the RF-110@IL catalyst undergoes self-degradation to release nitrogenous species. This is further supported by FT-IR analysis (Fig. S18), where the characteristic peaks of the imidazolium ring remain intact after the photocatalytic process. These findings confirm the structural integrity of RF-110@IL and verify that the ammonia yield originates solely from the catalytic reduction of atmospheric N_2. In a thermostatted apparatus (Fig. S1), RF-110 and RF-110@IL dissolved in deionized water were kept under illumination at 25 °C under a flow rate of 20 mL min^{-1} of high-purity nitrogen (99.99%). The evolution of the NH_3 production as a function of the time (Fig. 5A) indicates that (i) for both catalysts production appeared after 10 min and (ii) the production increased during the first hour. Both catalysts exhibited a slight loss in NH_3 conversion over a testing period of 2 h, which suggests stable catalytic activity. After 120 minutes of illumination, RF-110 produced only 32.6 μmol g^{-1} of NH_3, while RF-110@IL produced 58.7 μmol g^{-1}. The ammonia output by RF-110@IL in two hours was 1.80 times that of RF-110. These experimental results suggest that grafting ionic liquids promotes photocatalytic activity.

To improve the precision of the experimental results, we employed both the Nessler reagent and the indophenol blue methods to quantify ammonia concentrations (Fig. 5B and C). After 120 min of illumination using the Nessler reagent method, the NH_3 production rate was 29.4 μmol g^{-1} h^{-1} for RF-110@IL and 16.3 μmol g^{-1} h^{-1} for RF-110. The formation rate was 26.3 μmol g^{-1} h^{-1} for RF-110@IL and 14.3 μmol g^{-1} h^{-1} for RF-110 using the indophenol blue method. To evaluate the impact of ionic liquid modification on the durability of the catalyst, recycling tests were conducted for both bare RF-110 and RF-110@IL (Fig. 5D). Both materials displayed high stability over

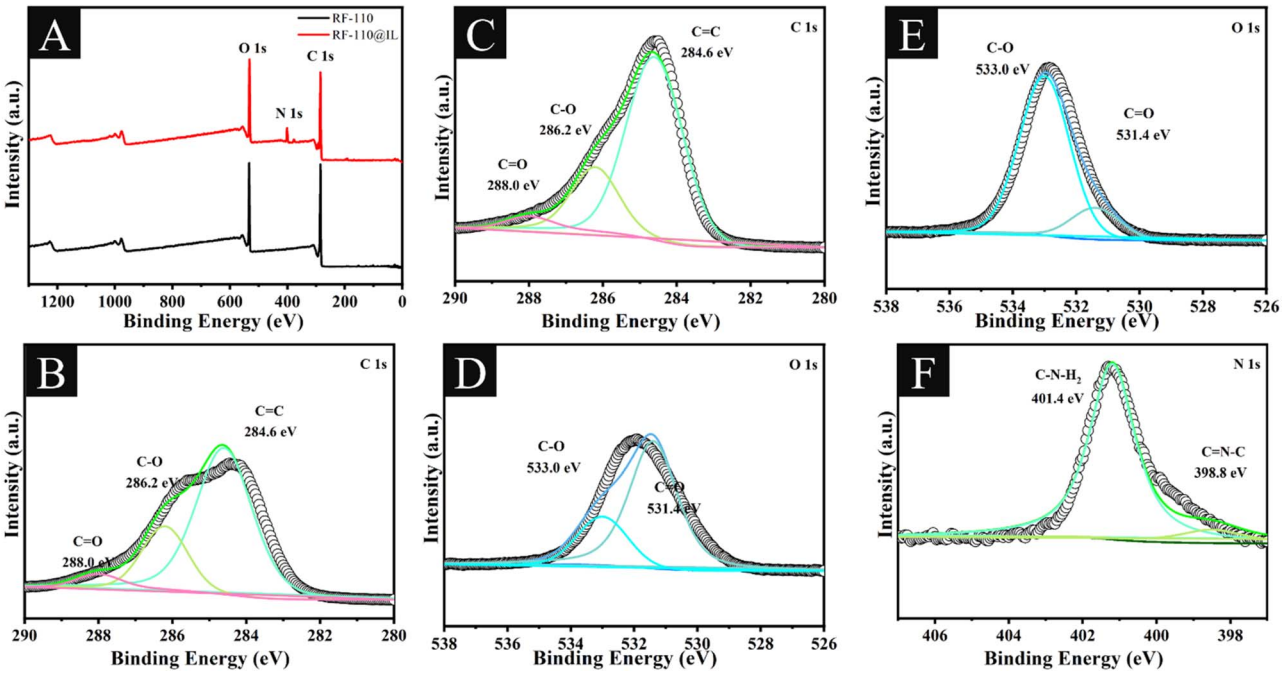

Fig. 4 (A) XPS survey spectra of RF-110 and RF-110@IL; (B and C) high-resolution C 1s and O 1s XPS spectra of RF-110, respectively; (D–F) high-resolution C 1s, O 1s and N 1s XPS spectra of RF-110@IL, respectively.

five cycles, with no significant decline in the NH_4^+ production rate. Notably, RF-110@IL consistently delivered a superior NH_4^+ yield (approx. 60 μmol g^{-1}) compared to the bare RF-110 (approx. 26 μmol g^{-1}) in each run. These results indicate that the IL layer is firmly anchored to the RF surface and retains its structural integrity, providing a durable and highly efficient interface for continuous photocatalytic nitrogen fixation.

At the same time, we carried out error experiments, and the findings revealed that the ammonia production in 3 experiments was not significantly different, suggesting the dependability of the experimental results.

To provide a comprehensive understanding of the photocatalytic process, the evolution of gaseous products was quantitatively monitored. As illustrated in Fig S19 and S20, the RF-110@IL catalyst exhibits simultaneous evolution of H_2 and O_2 during the nitrogen fixation reaction. The calibration curves for H_2 ($Y = 5.395 \times 10^{-10}X + 5.297 \times 10^{-9}$, $R^2 = 0.9997$) and O_2 ($Y = 6.04 \times 10^{-10}X + 1.158 \times 10^{-9}$, $R^2 = 0.9998$) ensure high precision in gas quantification. The detected O_2 yield (approximately 4.45×10^{-8} mol) provides direct experimental evidence for the water oxidation half-reaction. This confirms that the photogenerated holes in the valence band of the RF core are effectively consumed, providing the necessary protons and maintaining charge balance for the nitrogen reduction reaction.

To further investigate the catalytic selectivity, the competitive hydrogen evolution reaction (HER) was quantitatively monitored. As shown in Fig. S20, the pristine RF-110 exhibited a noticeable H_2 yield of 4.35 μmol g^{-1} (2.18×10^{-7} mol). In contrast, the RF-110@IL catalyst yielded a significantly suppressed amount of H_2 (approximately 1.20 μmol g^{-1}, 6.01×10^{-8} mol) alongside the enhanced ammonia production. Crucially, the IL coating serves as a selectivity regulator: by creating a localized environment with high N_2 solubility and controlled proton flux, it effectively inhibits excessive HER. This modulation ensures that photogenerated electrons are preferentially utilized for N_2 activation, increasing the NH_3/H_2 selectivity ratio by nearly 10-fold (from 5.0 to 50.1) compared to the unmodified RF-110.

The stability of RF-110@IL was also tested as shown in Fig. 5D. After five cycles, RF-110@IL showed no significant loss in its activity producing 54.4 μmol g^{-1} of NH_3 within 2 hours, retaining almost 95% of the ammonia created during the first photocatalytic reaction. These results indicate that RF-110@IL is robust and recyclable and has potential use in photocatalytic nitrogen reduction.

The light absorption performance and potential structure of RF-110@IL were examined using UV-Vis DRS and Mott–Schottky analysis. Fig. 6A exhibits a prominent broad diffraction peak at $2\theta = \sim 20°$ ($d = \sim 4.4$ Å) characteristic of the (002) plane of graphite carbon, confirming the presence of π-stacked aromatic structures in the resin.[38] Since RF-110@IL is an organic semiconductor with amorphous properties, there is a broad peak at $2\theta = \sim 20°$. After ionic liquid grafting, the peak shape does not change much. Fig. 6B depicts the UV-vis DRS spectra for RF-110 and RF-110@IL. It demonstrates that RF-110@IL has greater light absorption than RF-110, especially in the visible light band. It means ionic liquid grafting improves the light absorption capacity. Fig. 6C depicts the predicted band gap widths for RF-110 and RF-110@IL. RF-110 has a bandwidth of 1.95 eV while RF-110@IL has a bandwidth of 1.74 eV. Among them, RF-110@IL has a lower band gap width. Fig. 6D shows the material conduction band locations as determined by the Mott–

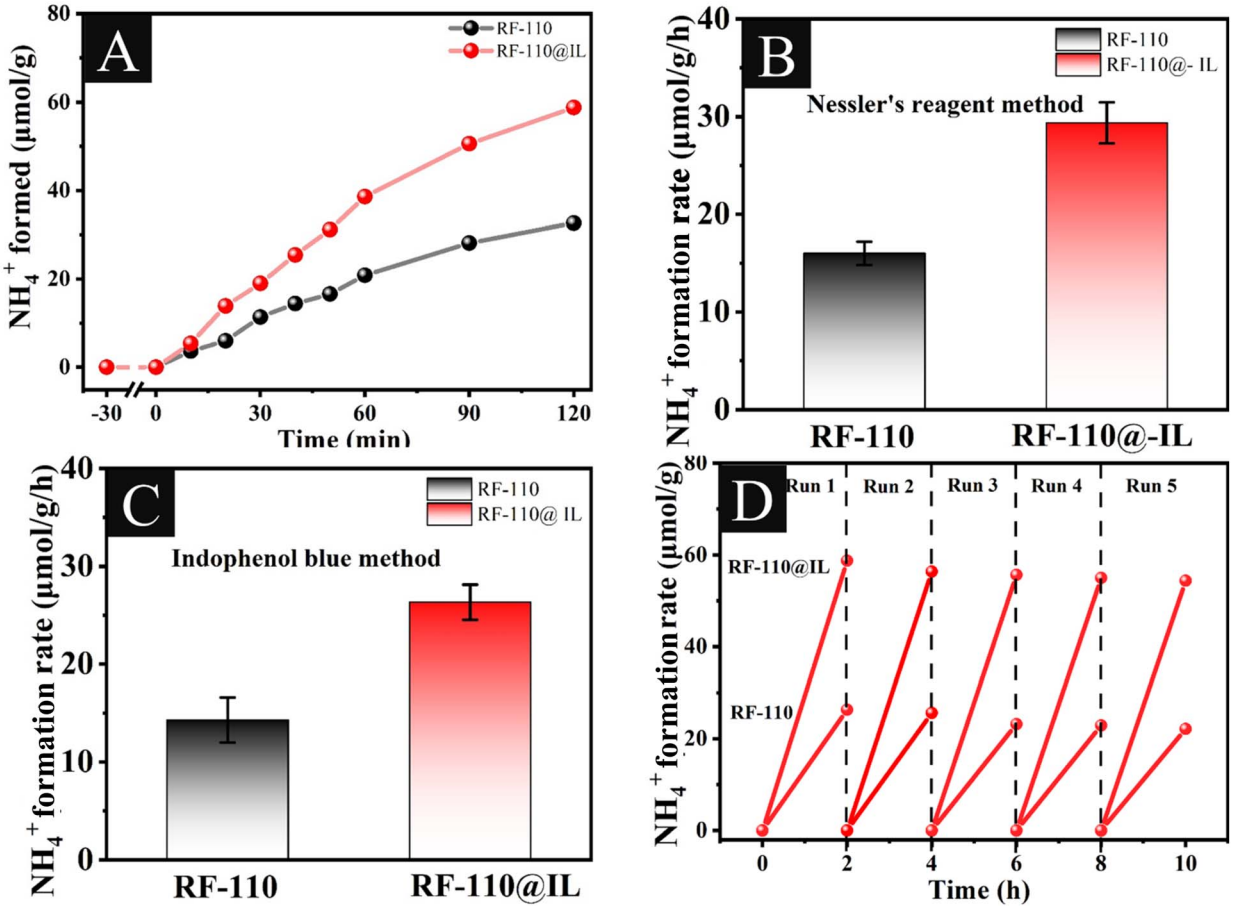

Fig. 5 (A) Photocatalytic NH_4^+ synthesis by RF-110 and RF-110@IL under simulated sunlight for different irradiation times; (B) NH_4^+ formation rate during photocatalytic nitrogen fixation for RF-110 and RF-110@IL under simulated sunlight during 120 min by the Nessler reagent method; (C) NH_4^+ formation rate during photocatalytic nitrogen fixation for RF-110 and RF-110@IL under simulated sunlight during 120 min by the indophenol blue method; (D) the recycling runs of the photocatalytic nitrogen reduction over RF-110@IL under simulated sunlight during 120 min.

Schottky test; the conduction band bottom is at −0.38 eV for RF-110 and at −0.46 eV for RF-110@IL.

The valence band of nanomaterials can be calculated using the equation $E_g = E_{VB} - E_{CB}$. For RF-110@IL, the computed position of the valence band top is at +1.28 eV while for RF-110 it is at +1.57 eV. As shown in Fig. 7A, the position of the valence band top is greater than the potential for H_2O oxidation to produce protons, and the conduction band bottom is more negative than the potential for nitrogen reduction (−0.99 eV) to make ammonia. Furthermore, the updated band structure potentials (CB and VB) demonstrate that RF-110@IL possesses appropriate redox abilities for both N_2 reduction and H_2O oxidation, which is in good agreement with our experimental observations of NH_4^+, H_2 and O_2 evolution. In general, it means that photogenerated electrons can successfully reduce nitrogen to produce ammonia with the protons from water. The potential structure demonstrates that RF-110@IL can be employed in the PCNRR, and the reaction process is described in Fig. 7B.

Electrochemical properties are investigated utilizing characterization techniques such as transient photocurrent densities, electrochemical impedance spectroscopy, photoluminescence spectra, and time-resolved fluorescence spectra.

As demonstrated in Fig. 8A, RF-110@IL has higher photocurrent intensity, implying more photogenerated electrons. The photocurrent response demonstrates that RF-110@IL has a greater current density than RF-110, showing that ionic liquid grafting efficiently promotes carrier separation. As shown in Fig. 8B, the fluorescence intensity of RF-110@IL is lower, indicating that when the material is excited by light, there is less photogenerated electron–hole recombination than with RF-110, resulting in stronger photocatalytic activity, which is beneficial to the photocatalytic reaction. The higher fluorescence intensity of RF-110 suggests that there is more photogenerated electron–hole recombination, which is not beneficial to photocatalytic activity.

As illustrated in Fig. 8C, the arc radius of RF-110@IL is much less than that of RF-110. The experimental results reveal that the resistance to carrier conduction following ionic liquid grafting is low, which efficiently promotes the separation of photogenerated electrons and holes, resulting in increased photocatalytic activity.

When exposed to an excitation light source, a fluorescent system releases fluorescence in all directions. When the light source stops irradiating, the fluorescence gradually fades to

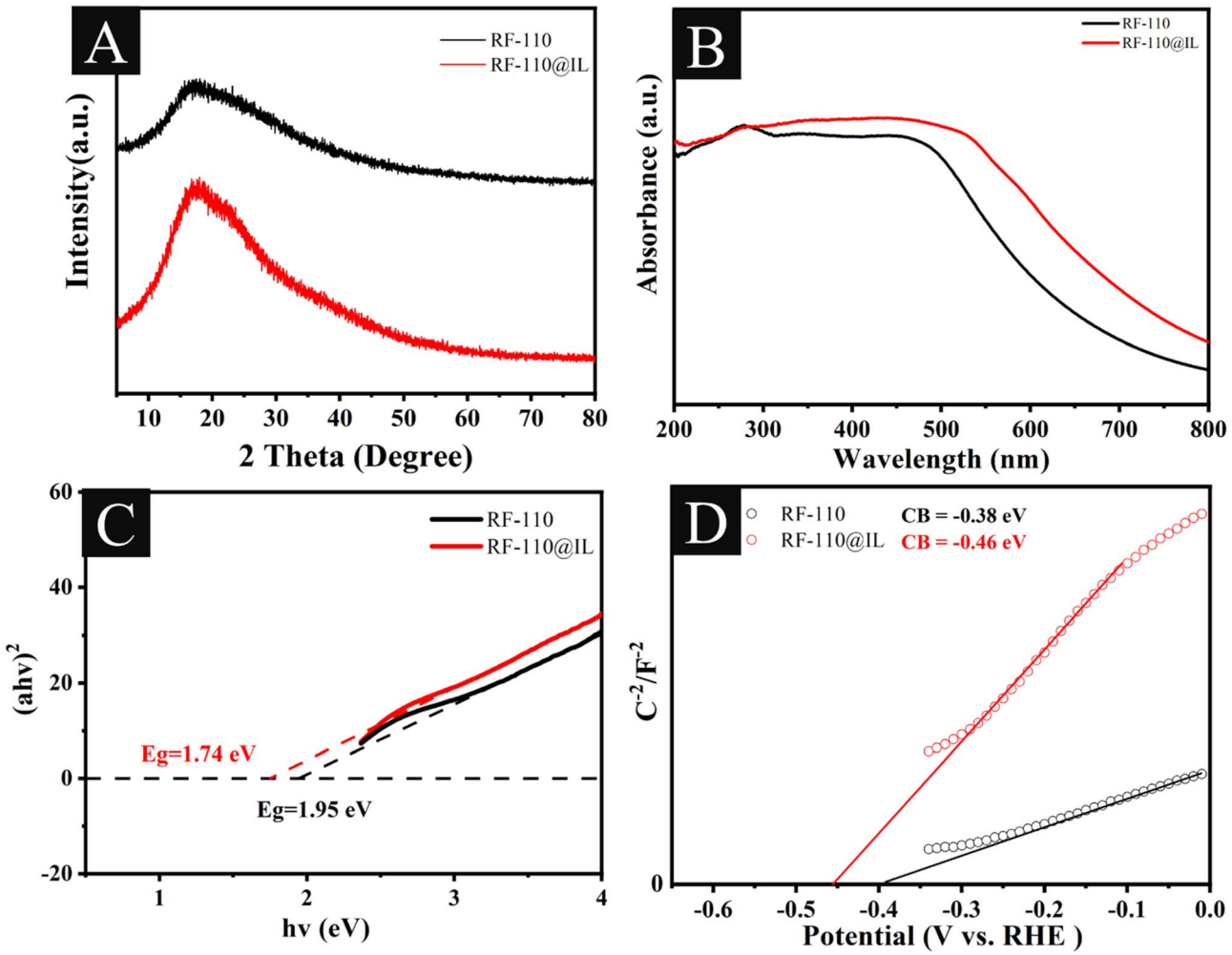

Fig. 6 (A) XRD images of RF-110 and RF-110@IL. (B) UV-Vis DRS spectra of RF-110 and RF-110@IL. (C) Band gap widths of RF-110 and RF-110@IL. (D) Mott–Schottky spectra of RF-110 and RF-110@IL.

zero. Fluorescence lifetime is the average time a molecule spends in an excited state before returning to its ground state after being excited by a light pulse. In the realm of photocatalysis, the fluorescence lifespan can be used to determine the efficiency of electron–hole pair separation. The greater the fluorescence lifespan, the longer the electron existence lifetime, which improves the electron–hole pair separation effect.

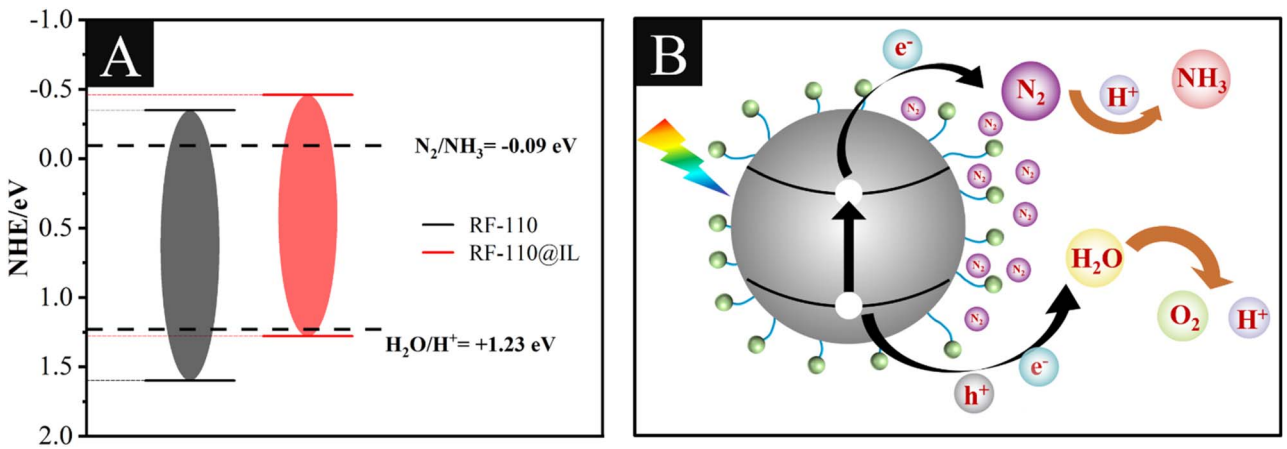

Fig. 7 (A) Potential structure spectra of RF-110 and RF-110@IL. (B) Photocatalytic nitrogen fixation reaction pathway.

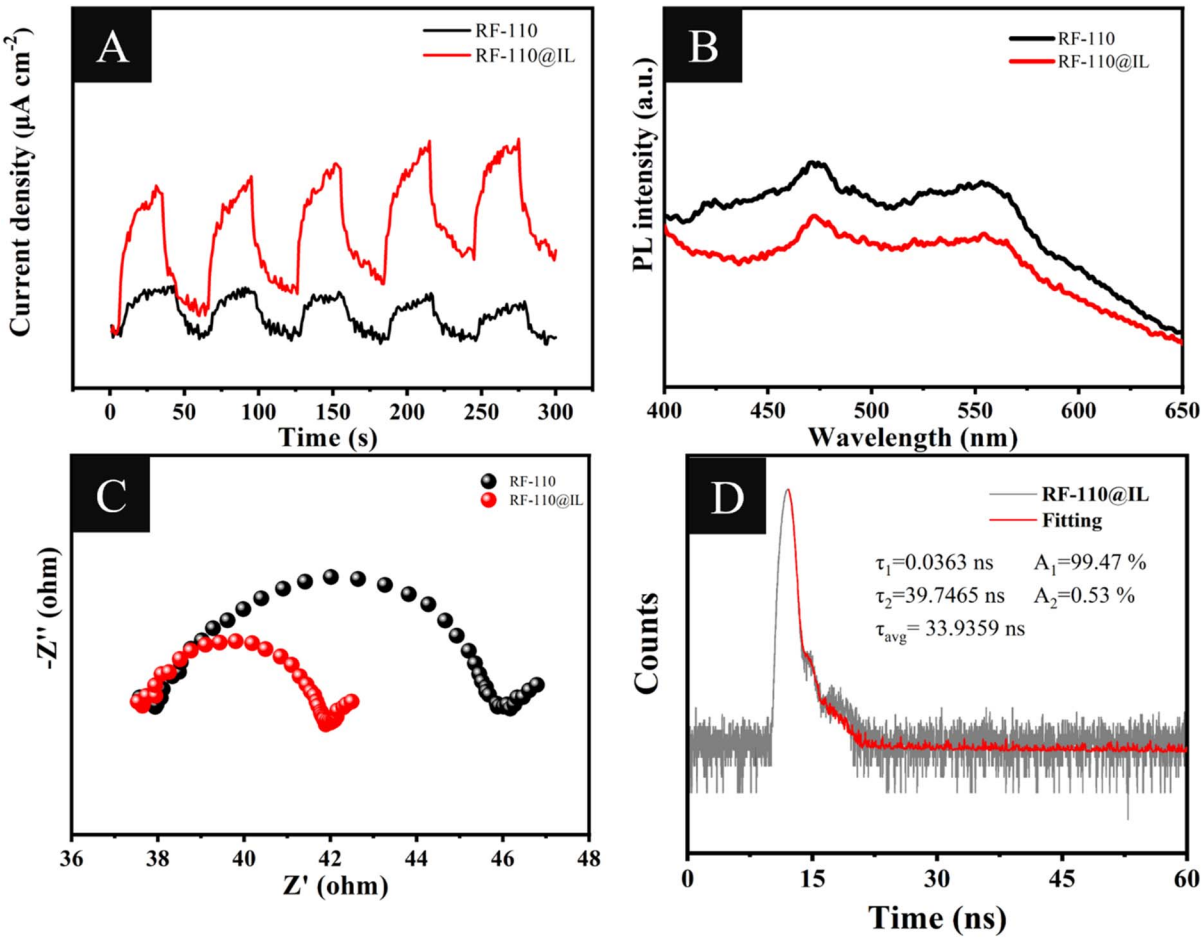

Fig. 8 (A) Transient photocurrent densities of RF-110 and RF-110@IL. (B) Photoluminescence spectra of RF-110 and RF-110@IL. (C) Electrochemical impedance spectroscopy of RF-110 and RF-110@IL. (D) Time-resolved fluorescence spectrum of RF-110@IL.

Fig. 8D and S21 show that the fluorescence lifetimes (τ_2) of RF-110 and RF-110@IL are 31.38 ns and 39.75 ns, respectively. The experimental results reveal that after ionic liquid grafting, the longer the electron existence time for photogenerated carriers, the greater the separation effect of electron–hole pairs. The above photoelectric characterization results all follow the same rule. Compared to RF-110, ionic liquid grafting is better at separating photogenerated carriers. These findings are consistent with the high photocatalytic activity of RF-110@IL.

4 Conclusions

In conclusion, we successfully grafted 1-methylimidazole-based IL onto RF-110 using 1,3-dibromopropane as a bridge. The experimental results were validated by XPS, FESEM mapping, EDX, and FT-IR analyses. We used RF-110@IL in the photocatalytic nitrogen fixation experiment. Two detection methods confirmed an ammonia production rate of 29.4 μmol g^{-1} h^{-1}, 1.8 times higher than that obtained when using RF-110. The results revealed that grafting with ionic liquids can significantly boost photocatalytic nitrogen fixation performance. In the investigation of photoelectrochemical properties, we assessed the experimental data and confirmed that the RF-110@IL catalyst generated after ionic liquid grafting had good photoelectrochemical properties, which also explains the increase in photocatalytic nitrogen fixation activity. As shown in S22, we can conclude that the addition of ionic liquids to the photocatalytic nitrogen fixation reaction can significantly boost photocatalytic nitrogen fixation activity, which is extremely important for our research into RF modification.

Author contributions

Ning Zhang performed all the experiments and wrote the manuscript. Dorian Priano assisted with the TEM test. Catherine Santini, Jinlong Zhang and Stephane Daniele revised the manuscript. All authors discussed the results and provided comments on the manuscript.

Conflicts of interest

There are no conflicts to declare.

Data availability

The authors confirm that the data supporting the findings of this study are available within the article and its supplementary

information (SI). Supplementary information is available. See DOI: https://doi.org/10.1039/d5se01680k.

Acknowledgements

Ning Zhang thanks the China Scholarship Council (CSC) for PhD funding. The authors acknowledge financial support from the French National Research Agency (ANR) under the France 2030 program and reference ANR-21-PEHD-00XX-04 (project PEPRH2-GREENH3).

Notes and references

1 Y. Ran, X. Yu, J. Liu, J. Cui, J. Wang, L. Wang, Y. Zhang, X. Xiang and J. Ye, *J. Mater. Chem. A*, 2020, **8**, 13292–13298.
2 S. Z. Andersen, V. Colic, S. Yang, J. A. Schwalbe, A. C. Nielander, J. M. McEnaney, K. Enemark-Rasmussen, J. G. Baker, A. R. Singh, B. A. Rohr, M. J. Statt, S. J. Blair, S. Mezzavilla, J. Kibsgaard, P. C. K. Vesborg, M. Cargnello, S. F. Bent, T. F. Jaramillo, I. E. L. Stephens, J. K. Norskov and I. Chorkendorff, *Nature*, 2019, **570**, 504–508.
3 J. G. Chen, R. M. Crooks, L. C. Seefeldt, K. L. Bren, R. M. Bullock, M. Y. Darensbourg, P. L. Holland, B. Hoffman, M. J. Janik, A. K. Jones, M. G. Kanatzidis, P. King, K. M. Lancaster, S. V. Lymar, P. Pfromm, W. F. Schneider and R. R. Schrock, *Science*, 2018, **360**, eaar6611.
4 G.-L. Hu, Y.-J. Lei, R. Hu, H.-M. Sun, Q. Gu, D.-Z. Ren and H.-Y. Wang, *Int. J. Hydrogen Energy*, 2019, **44**, 31884–31891.
5 Y. Hu, S. Du, J. Lang, H. Liu, X. Li, Q. Zhang, M. Lu, X. Li, B. Li, M. Wei and L. Yang, *Chin. J. Catal.*, 2026, **81**, 227–245.
6 X. C. Tang, Z. Ding, Z. H. Wang, N. Arif, Y. Y. Chen, L. Li and Y. J. Zeng, *ChemCatChem*, 2024, **16**, e202401355.
7 Y. Li, *Langmuir*, 2025, **41**, 23253–23272.
8 T. Zhang, X. Zhang and F. Chang, *Ind. Eng. Chem. Res.*, 2025, **64**, 14879–14887.
9 P. Li, Y. Gao, A. G. L. Borthwick, P. Li, H. Zhang, F. Chen, L. Chen, F. Li and W. Liu, *Angew Chem. Int. Ed. Engl.*, 2025, **64**, e202503097.
10 X. Wang, R. Gao, G. Fan, Y. Guo, C. Han, Y. Gao, A. Shen, L. Wu and X. Gu, *Angew Chem. Int. Ed. Engl.*, 2025, **64**, e202501297.
11 T. Y. Chen, Y. R. Ying, J. Wu, X. H. Liu and H. Huang, *Angew Chem. Int. Ed. Engl.*, 2025, **64**, e202509705.
12 Y. Zhang, X. Yu, Z. Gong, Y. Mi, M. Liu, L. Wang and S. Zeng, *Appl. Surf. Sci.*, 2025, **700**, 163100.
13 S. Wu, Z. Chen, K. Liu, W. Yue, L. Wang and J. Zhang, *ChemSusChem*, 2020, **13**, 3455–3461.
14 Y. Sun, J. Chen, A. Luo, Y. Sun, Z. Deng, W. Sun and L. Xu, *J. Environ. Chem. Eng.*, 2025, **13**, 118191.
15 Y. Qu, W. Ma, S. Lei, Y. Yu, D. Sun, H. Du and M. Ren, *J. Alloys Compd.*, 2025, **1044**, 184499.
16 R. W. PEKALA, *J. Mater. Sci.*, 1989, **24**, 3221–3227.
17 G. Zhang, C. Ni, L. Liu, G. Zhao, F. Fina and J. T. S. Irvine, *J. Mater. Chem. A*, 2015, **3**, 15413–15419.
18 Y. Shiraishi, Y. Nishiyama, T. Jono, S. Tanaka and T. Hirai, *ACS Appl. Mater. Interfaces*, 2025, **17**, 56197–56204.
19 Y. Shiraishi, T. Takii, T. Hagi, S. Mori, Y. Kofuji, Y. Kitagawa, S. Tanaka, S. Ichikawa and T. Hirai, *Nat. Mater.*, 2019, **18**, 985–993.
20 M. Y. Balogun, P. J. Thacker, L. M. Cañada and J. F. Brennecke, *Ind. Eng. Chem. Res.*, 2025, **64**, 20729–20743.
21 Z. Song, J. Chen, J. Cheng, G. Chen and Z. Qi, *Chem. Rev.*, 2024, **124**, 248–317.
22 S. Stevanovic and M. F. Costa Gomes, *J. Chem. Therm.*, 2013, **59**, 65–71.
23 X. Gong, W. Teng, W. Liu, H. Xiao, H. Li, H. Ou and G. Yang, *Adv. Mater.*, 2025, **37**, 12924.
24 B. H. R. Suryanto, C. S. M. Kang, D. Wang, C. Xiao, F. Zhou, L. M. Azofra, L. Cavallo, X. Zhang and D. R. MacFarlane, *ACS Energy Lett.*, 2018, **3**, 1219–1224.
25 X. Gong, B. Chong, M. Xia, H. Li, H. Ou and G. Yang, *Catal. Sci. Technol.*, 2024, **14**, 343–352.
26 M. Yin, L. Wang and S. Tang, *ACS Appl. Mater. Interfaces*, 2022, **14**, 55674–55685.
27 V. Renuga, A. Manikandan, C. Neela Mohan, B. Meenatchi and B. Ganga, *J. Mol. Liq.*, 2017, **244**, 65–76.
28 Y. Zhao, H. Wang, L. Zeng and L. Huang, *J. Mater. Chem. A*, 2025, **13**, 5546–5560.
29 J. Dupont, B. C. Leal, P. Lozano, A. L. Monteiro, P. Migowski and J. D. Scholten, *Chem. Rev.*, 2024, **124**, 5227–5420.
30 X. Chen, H. Sun, J. Zhang, Y. Guo and D.-H. Kuo, *J. Mol. Liq.*, 2019, **273**, 50–57.
31 A. Golabiewska, M. Paszkiewicz-Gawron, A. Sadzinska, W. Lisowski, E. Grabowska, A. Zaleska-Medynska and J. Luczak, *Beilstein J. Nanotechnol.*, 2018, **9**, 580–590.
32 Y. Peng, K. C. Szeto, C. C. Santini and S. Daniele, *Chem. Eng. J. Adv.*, 2022, **12**, 100379.
33 J. Qiu, Y. Zhao, Z. Li, H. Wang, Y. Shi and J. Wang, *ChemSusChem*, 2019, **12**, 2421–2427.
34 J. Liu, S. Z. Qiao, H. Liu, J. Chen, A. Orpe, D. Zhao and G. Q. Lu, *Angew Chem. Int. Ed. Engl.*, 2011, **50**, 5947–5951.
35 B. H. R. Suryanto, K. Matuszek, J. Choi, R. Y. Hodgetts, H.-L. Du, J. M. Bakker, C. S. M. Kang, P. V. Cherepanov, A. N. Simonov and D. R. MacFarlane, *Science*, 2021, **372**, 1187–1191.
36 J. Li, J. Huang, G. Zeng, C. Zhang, H. Yu, Q. Wan, K. Yi, W. Zhang, H. Pang, S. Liu, S. Li and W. He, *Chem. Eng. J.*, 2023, **463**, 142512.
37 C. B. Park and B. J. Sung, *J. Phys. Chem. B*, 2020, **124**, 6894–6904.
38 L. Wang, W. Wu, W. Zhang, X. Ren, X. Liu, W.-K. Ho, J. Hu and M. Zhou, *J. Mater. Chem. A*, 2025, **13**, 31112–31121.